

# Open Research Online

---

The Open University's repository of research publications and other research outputs

## Kyanite petrogenesis in migmatites: resolving melting and metamorphic signatures

### Journal Item

#### How to cite:

Phillips, Stacy E.; Argles, Tom W.; Warren, Clare J.; Harris, Nigel B. W. and Kunz, Barbara E. (2023). Kyanite petrogenesis in migmatites: resolving melting and metamorphic signatures. *Contributions to Mineralogy and Petrology*, 178(2), article no. 10.

For guidance on citations see [FAQs](#).

© 2023 The Authors



<https://creativecommons.org/licenses/by/4.0/>

Version: Version of Record

Link(s) to article on publisher's website:

<http://dx.doi.org/doi:10.1007/s00410-022-01991-w>

---

Copyright and Moral Rights for the articles on this site are retained by the individual authors and/or other copyright owners. For more information on Open Research Online's [data policy](#) on reuse of materials please consult the policies page.

---

[oro.open.ac.uk](http://oro.open.ac.uk)



# Kyanite petrogenesis in migmatites: resolving melting and metamorphic signatures

Stacy E. Phillips<sup>1</sup> · Tom W. Argles<sup>1</sup> · Clare J. Warren<sup>1</sup> · Nigel B. W. Harris<sup>1</sup> · Barbara E. Kunz<sup>1</sup>

Received: 24 July 2021 / Accepted: 20 December 2022  
© The Author(s) 2023

## Abstract

Aluminosilicates (kyanite, sillimanite and andalusite) are useful pressure–temperature (P–T) indicators that can form in a range of rock types through different mineral reactions, including those that involve partial melting. However, the presence of xenocrystic or inherited grains may lead to spurious P–T interpretations. The morphologies, microtextural positions, cathodoluminescence responses and trace element compositions of migmatite-hosted kyanite from Eastern Bhutan were investigated to determine whether sub-solidus kyanite could be distinguished from kyanite that crystallised directly from partial melt, or from kyanite that grew peritectically during muscovite dehydration reactions. Morphology and cathodoluminescence response were found to be the most reliable petrogenetic indicators. Trace element abundances generally support petrographic evidence, but protolith bulk composition exerts a strong control over absolute element abundance in kyanite. Sample-normalised concentrations show distinctive differences between petrogenetic types, particularly for Mg, Ti, V, Cr, Mn, Fe and Ge. LA-ICP-MS element maps, particularly combined to show Cr/V, provide additional information about changing geochemical environments during kyanite growth. Most kyanite in the studied migmatitic leucosomes is of sub-solidus origin, with less widespread evidence for peritectic crystallisation. Where present, grain rims commonly crystallised directly from the melt; however, entire grains crystallised exclusively from melt are rare. The presence of kyanite in leucosomes does not, therefore, necessarily constrain the P–T conditions of melting, and the mechanism of growth should be determined before using kyanite as a P–T indicator. This finding has significant implications for the interpretation of kyanite-bearing migmatites as representing early stages of melting during Himalayan evolution.

**Keywords** Kyanite · Migmatite · Trace elements · LA-ICP-MS · Cathodoluminescence

## Introduction

Aluminosilicate phases are commonly used to provide broad constraints on the pressure–temperature (P–T) conditions reached by a wide range of metamorphic and anatectic rocks, with kyanite suggesting high-P, sillimanite high-T, and andalusite low-P conditions. In sub-solidus metasedimentary rocks, aluminosilicates can form through a variety of discontinuous and continuous mineral reactions. During partial melting reactions and the subsequent formation of migmatites, aluminosilicates may form from incongruent

melting as peritectic products, may crystallise directly from melt, or may occur in melt portions as xenocrysts inherited from the metamorphic source. Each sub-or supra-solidus petrogenesis, therefore, has different implications for the metamorphic evolution of the host rock.

The presence of a particular aluminosilicate polymorph plays a critical role in the interpretation of orogenic processes. The presence (or absence) of sub-solidus kyanite and sillimanite has been used across the Himalayan orogen to constrain the P–T conditions of high-grade rocks (Hodges 2000 and references therein). The presence of kyanite in Himalayan leucogranites is commonly interpreted as a sign of melting during prograde (high-P) burial (Groppo et al. 2010; Iaccarino et al. 2015); in contrast, the more widespread sillimanite-bearing leucogranites are generally interpreted as the products of later melting related to decompression during exhumation (Harris and Massey 1994; Weinberg 2016). The location and age of granite bodies and

---

Communicated by Daniela Rubatto.

✉ Stacy E. Phillips  
stacyphillips429@gmail.com

<sup>1</sup> School of Environment, Earth and Ecosystems Science, The Open University, Milton Keynes MK7 6AA, UK

migmatites containing either kyanite or sillimanite therefore underpins evolutionary models of Himalayan formation (i.e. the channel flow model of Beaumont et al. 2001), providing evidence for prograde or decompression melting. Evaluating the petrogenetic history of kyanite in these rocks is therefore critical for constraining tectonic models of orogenic evolution in general, and models of Himalayan evolution in particular.

One of the ways in which kyanite petrogenesis may be investigated is through specialised imaging and detailed geochemical analyses. Kyanite can incorporate 100's–1000's ppm of Fe, V, Cr and Ti as well as lower concentrations of other trace elements (Albee and Chodos 1969; Chinner et al. 1969; Deer et al. 2013; Herz and Dutra 1964; Neiva 1984; Pearson and Shaw 1960; Yang and Rivers 2001). How these elements vary within kyanite grains, however, is poorly understood. Studies of sub-solidus rocks have suggested that kyanite preserves growth zoning through (poly-)metamorphic cycles (Peterman et al. 2021). CL imagery of kyanite has been shown to reveal subtle textural details that have been linked to trace element variations (Horkley et al. 2013; Kendrick and Indares 2017; Müller

et al. 2016; Peterman et al. 2021; Schertl et al. 2004; Taran-tola et al. 2019). Different elements may act as CL quenchers or activators: Cr and Ti, for example, are known to be CL activators, whereas Fe is a known CL quencher (Gaft et al. 2015; Habermann 2002; Pagel et al. 2000; Wojtowicz 1991). Variations in the concentrations of these elements have been shown to correlate well with changes in CL intensity (Müller et al. 2003). Maps produced by LA-ICP-MS allow quantification of spatial variability in trace element concentrations that are too low to be resolved by electron microprobe—these types of maps have previously been used to investigate chemical zoning in pyroxene, amphibole, and garnet (George et al. 2018; Raimondo et al. 2017; Ubide et al. 2015; Ulrich et al. 2009).

Here, we characterise the petrographic and geochemical composition of kyanite in metapelitic migmatites in Eastern Bhutan (Fig. 1). This region provides good exposure of a sequence of kyanite-grade rocks over a thickness of hundreds of metres (Grujic et al. 2002). Changes in kyanite composition were investigated using a combination of optical petrography, CL imaging, electron microprobe spot analyses, LA-ICP-MS maps (the first instance of this technique

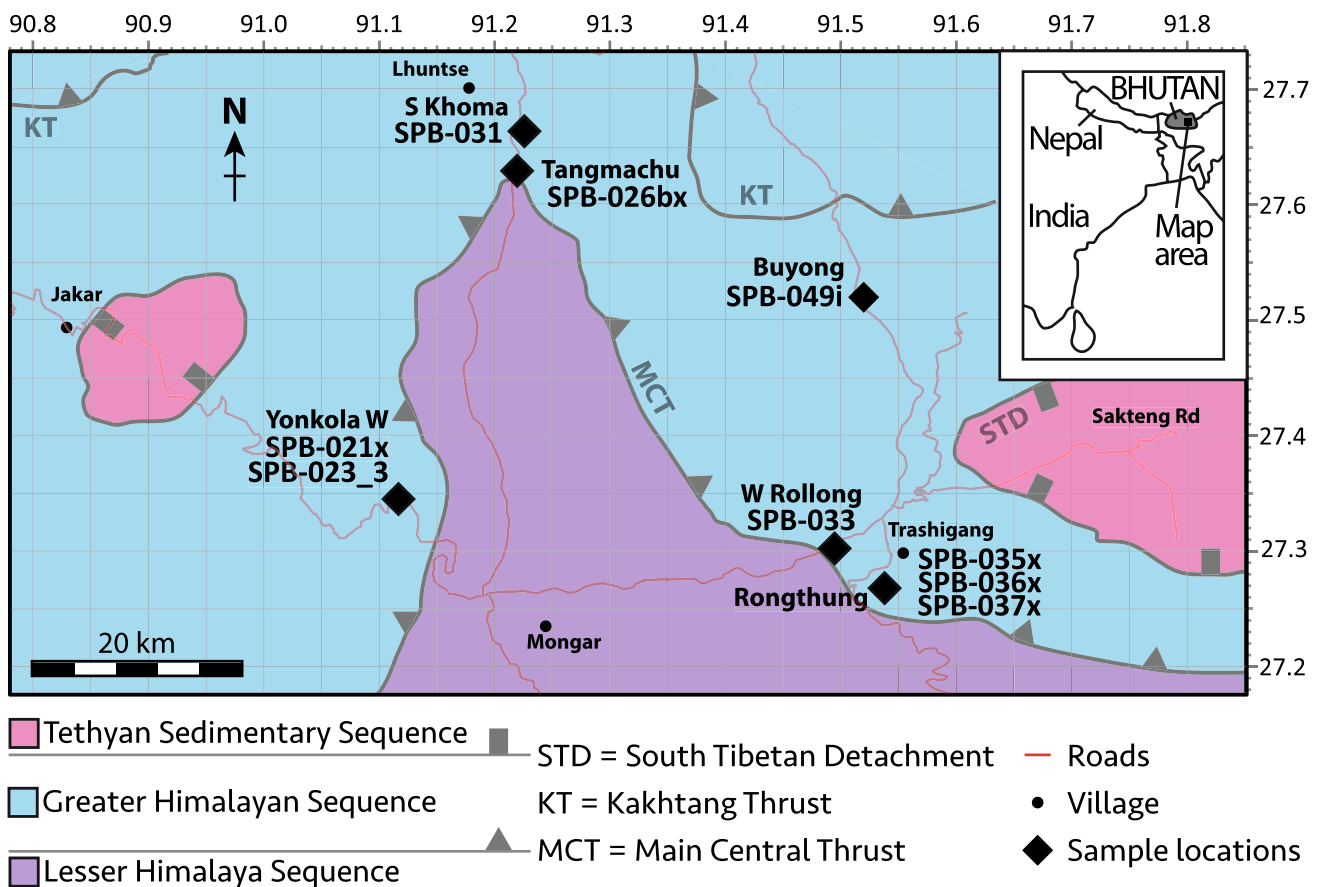


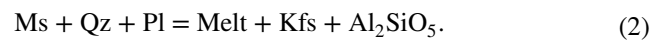
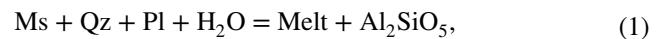
**Fig. 1** Map of sample locations in E Bhutan. Redrawn after Greenwood et al. (2015). Map projection is WGS84, latitude and longitude in decimal degrees. Coordinates for sample locations are provided alongside samples in Table 1

being applied to kyanite), and LA-ICP-MS spot analyses. Our results document microstructurally and geochemically distinct zones in kyanite that can be linked to growth during sub-solidus, peritectic and supra-solidus reactions. The identification of xenocrystic kyanite suggests that the presence of kyanite in a migmatite or granite alone does not necessarily constrain the P–T conditions of melt formation. As many previous studies have interpreted the presence of kyanite in leucosomes as evidence for the earliest stages of melting in the Himalaya, re-evaluation of these instances based on our observations may be needed.

### Metamorphism and partial melting in the Himalaya

The Himalayan orogen formed as a result of the collision of the Indian and Eurasian continents that started approximately 50 Ma ago and is ongoing today (Hodges 2000; Najman et al. 2010). The metamorphic core of the Himalaya (the Greater Himalayan Sequence or GHS) comprises metapelites and orthogneisses metamorphosed to amphibolite- and granulite facies conditions, which represent the metamorphosed strata of a sedimentary wedge deposited on the Indian margin, as well as remnants of the underlying Indian lower crustal rocks (Cottle et al. 2015). During the collision, widespread metamorphism and partial melting affected the buried Indian continental crust.

In Bhutan, the GHS is divided into lower and upper units by a somewhat cryptic structure: the Kakhtang Thrust (Davidson et al. 1997; Grujic et al. 2002). In Eastern Bhutan, the Lower GHS generally comprises kyanite-grade mica schists and gneisses with occasional migmatites; kyanite-grade migmatites have also been reported in the structurally lowest parts of the Upper GHS (Daniel et al. 2003 as cited in Harris et al. 2004). At structurally higher levels towards the Kakhtang Thrust, kyanite–sillimanite gneisses with an increasing abundance of leucogranite sills and dykes are exposed. Peak P–T conditions of 0.8–1.2 GPa/650–700 °C were reached in the Lower GHS immediately above the Main Central Thrust (MCT), the pan-orogen structure that separates the GHS from the underlying lower grade unit, increasing to 1.0–1.4 GPa/750–800 °C 500 m above the MCT at ~23 Ma (Daniel et al. 2003). The GHS preserves widespread evidence for partial melting in the form of migmatites and peraluminous (commonly sillimanite-bearing) leucogranite bodies dated between 24 and 10 Ma (Harrison et al. 1997). Granite formation is generally attributed to muscovite dehydration melting of GHS metapelitic assemblages that occurred as a result of decompression within the sillimanite field during metamorphism along clockwise P–T paths (Dasgupta et al. 2009; Harris and Massey 1994; Harrison et al. 1999; Rubatto et al. 2013; Visonà et al. 2012). This muscovite breakdown occurs through one of the following reactions:



In both reactions, the aluminosilicate (usually sillimanite) is formed as a peritectic phase (Dyck et al. 2020; Harris and Inger 1992); sillimanite may also crystallise directly from the melt (Zen 1988).

The GHS preserves widespread evidence for partial melting in the form of migmatites and peraluminous leucogranite bodies, with many migmatites being dated at > 24 Ma (Groppo et al. 2010; Iaccarino et al. 2015; Imayama et al. 2012; King et al. 2011; Lee et al. 2004; Prince et al. 2001; Rubatto et al. 2013). Crucially a number of these migmatites, and especially those which contain kyanite, have been cited as evidence for melting under kyanite-grade conditions (Carosi et al. 2015; Iaccarino et al. 2015; Imayama et al. 2012; Godin et al. 2001; Groppo et al. 2010; Guilmette et al. 2011; Harris et al. 2004; Hodges et al. 1996). The implication of these observations is that these particular melts formed along the prograde path rather than along the retrograde path during decompression. In the Lower GHS of Bhutan however, kyanite-bearing migmatites exposed just above the MCT appear to be much younger, at 18–16 Ma (Daniel et al. 2003), suggesting either that the timing of exhumation may not be consistent within the GHS, or orogen-wide (Carosi et al. 2018).

### Field descriptions

Nine migmatite samples were collected from the Lower GHS in six different locations in Eastern Bhutan (Fig. 1, Table 1). All but one of the samples were collected within the structurally lowermost part of the Lower GHS, in the immediate hanging wall of the MCT. Sample SPB-049i was collected from a structurally higher locality within the Lower GHS, but still in the footwall of the Kakhtang Thrust. Field observations suggest a strong protolith control on the presence of melt, with increased evidence of melting in more pelitic versus more psammitic regions or layers.

The migmatites comprise discontinuous pale-coloured quartzo-feldspathic layers (leucosome) containing varying proportions of muscovite + kyanite within a more biotite-rich matrix (melanosome). The terms leucosome and melanosome are used throughout this contribution as purely descriptive terms, based generally on colour or abundance of felsic minerals vs. mafic minerals, respectively. All samples are from deformed leucosomes that are typically no bigger than 10 cm and are associated with two-mica ± garnet ± tourmaline schists (Fig. 2a). Some 30–50% of the leucosomes are in pinch-and-swell forms or are boudinaged, but all are concordant with the foliation of the host schists.

**Table 1** Mineralogy and sample locations of key kyanite-bearing samples, and the types of kyanite found in them, that are discussed further in the text

| Latitude | Longitude | Location  | Sample     | Rock type | Mineralogy  | Kyanite types |               |          |           |
|----------|-----------|-----------|------------|-----------|---|---------------|---------------|----------|-----------|
|          |           |           |            |           |   | Tabular       | Pokiloblastic | Corroded | Prismatic |
| 27.3499  | 91.1091   | Yonkola   | SPB-021x   | Paleosome | Pl, Qz, Ms, Bt, Grt, Ky, Chl (retrograde), Ilm, Ru, Mnz, Zrn                              | x             |               |          |           |
|          |           | Yonkola   | SPB-021x   | Leucosome | Pl, Qz, Kfs, Ms, Bt (schlieren), Grt (schlieren), Ky, Chl (retrograde), Ilm, Ru, Mnz, Zrn | x             |               | x        | x         |
|          |           | Yonkola   | SPB-021xii | Leucosome | Pl, Qz, Kfs, Ms, Bt (schlieren), Ky, Ap, Mnz, Zrn   | x             |               | x        | x         |
|          |           | Yonkola   | SPB-023    | Paleosome | Pl, Qz, Ms, Bt, Ky, Tur, Mnz, Zrn   | x             |               |          |           |
|          |           | Yonkola   | SPB-023    | Leucosome | Pl, Qz, Ms, Bt (schlieren), Ky, Tur, Mnz, Zrn   | x             |               |          |           |
| 27.614   | 91.2125   | Tangmachu | SPB-026bx  | Paleosome | Pl, Qz, Ms, Bt, Grt, Ky, St (rare), Ilm, Ru, Mnz, Zrn                                     | x             |               |          |           |
|          |           | Tangmachu | SPB-026bx  | Leucosome | Pl, Qz, Kfs, Ms, Bt (schlieren), Grt (schlieren), Ky, Sil, Mnz, Zrn                       | x             |               |          |           |
| 27.6691  | 91.2175   | S Khoma   | SPB-031    | Paleosome | Pl, Qz, Bt, Grt, Ky, Ilm, Mnz, Zrn  | x             |               |          |           |
|          |           | S Khoma   | SPB-031    | Leucosome | Pl, Qz, Kfs, Ms, Bt (schlieren), Ky, Ilm, Mnz, Zrn  | x             | Rare          |          | Rare      |
| 27.3066  | 91.4888   | W Rollong | SPB-033    | Paleosome | Pl, Qz, Ms, Bt, Grt, Ky, Tur (rare), Ilm, Ru, Mnz, Zrn                                    | x             |               |          |           |
|          |           | W Rollong | SPB-033    | Leucosome | Pl, Qz, Kfs, Ms, Bt (schlieren), Grt, Ky, Ilm, Ru, Mnz, Zrn                               | x             |               | x        |           |
| 27.2723  | 91.5314   | Rongthung | SPB-035x   | Paleosome | Qz, Ms, Bt, Grt, Ky, Tur, Chl (retrograde), Ilm, Mnz, Zrn                                 | x             |               |          |           |
|          |           | Rongthung | SPB-035x   | Leucosome | Pl, Qz, Kfs, Ms, Bt, Grt, Ky, Sil, Chl (retrograde), Ilm, Mnz, Zrn                        | x             |               | x        |           |
|          |           | Rongthung | SPB-035xii | Paleosome | Pl, Qz, Ms, Bt, Grt, Ky, Sil, Tur, St (rare), Chl (retrograde), Ilm, Mnz, Zrn             | x             |               |          |           |
|          |           | Rongthung | SPB-036x   | Paleosome | Qz, Ms, Bt, Grt, Ky, Tur, Ilm, Ru, Mnz, Zrn   | x             |               |          |           |
|          |           | Rongthung | SPB-036x   | Leucosome | Pl, Qz, Kfs, Ms, Bt, Grt (schlieren), Ky, Ap, Ilm, Ru, Mnz, Zrn                           | x             |               | x        | Rare      |
|          |           | Rongthung | SPB-037x   | Paleosome | Qz, Ms, Bt, Grt, Ky, Tur, Ilm, Ru, Mnz, Zrn   | x             |               |          |           |
|          |           | Rongthung | SPB-037x   | Leucosome | Pl, Qz, Kfs, Ms, Bt, Grt (schlieren), Ky, Ilm, Ru, Mnz, Zrn                               | x             |               | x        |           |
|          |           | Rongthung | SPB-037x   | Leucosome | Pl, Qz, Kfs, Ms, Bt, Grt (schlieren), Ky, Ilm, Ru, Mnz, Zrn                               | x             |               | x        |           |
| 27.5238  | 91.5128   | Buyong    | SPB-049i   | Leucosome | Pl, Qz, Kfs, Ms, Bt, Ky, Ap, Ilm, Ru, Mnz, Zrn  |               | x             |          |           |

Mineral abbreviations according to Whitney and Evans (2010)

Leucosome volume in any given outcrop is variable, but is typically < 20%. No granitic dykes, veinlets, or feeder channels cross-cut the foliation, suggesting little evidence of melt migration beyond a scale of tens of metres. Kyanite is present in both the leucosome and the melanosome, with crystals ranging in size from < 1 cm up to 4 cm (Fig. 2a–c).

Migmatite style, melanosome composition, and leucosome volume vary on the hand-sample scale between samples. The spectrum of sample styles is shown in Fig. 2. In the

most segregated sample (SPB-023\_3; Fig. 2a, d) biotite- and tourmaline-rich restitic-melanosome is in sharp contact with the leucosome, which contains very rare biotite. In many samples, the melanosome resembles the composition of the paleosome (unmelted host rock schist) (Fig. 2b), and cm-sized rafts of biotite ± garnet schlieren are found in the leucosome (Fig. 2e). Melanosome–leucosome contacts are more diffuse and more difficult to distinguish in less-segregated samples; in end-member samples (such as SPB-049i)

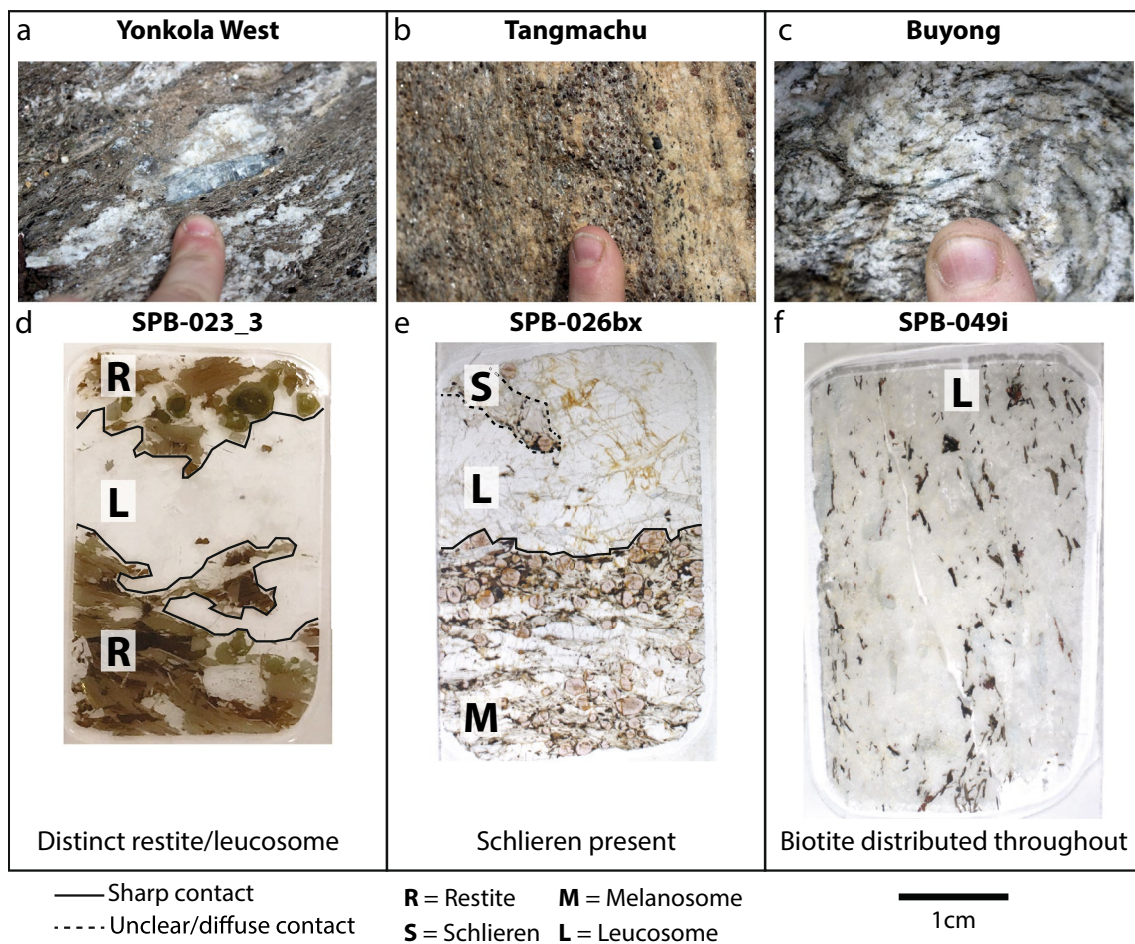


**Fig. 2** Field photographs and thin section photographs illustrating the range of migmatite types across E Bhutan, classified by the degree of segregation and distribution of biotite schlieren. **a** Outcrop at Yonkola West with irregular leucosome lenses in a kyanite-bearing schist, with large kyanite at the contact. **b** Leucocratic patches in garnet-rich kyanite schist at Tangmachu. **c** Nose of a tightly folded biotite-rich leucosome at Buyong. **d** Sample SPB-023\_3 (taken from

location shown in **(a)**) showing a distinctive segregation between biotite + tourmaline-rich restite and leucosome. **e** Sample SPB-026bx (taken from location shown in **(b)**) has a distinctive leucosome–melanosome margin and biotite-garnet schlieren. **f** Sample SPB-049i (taken from location shown in **(c)**) with variable amounts of biotite distributed throughout the leucosome

individual biotite grains are distributed throughout the leucosome (Fig. 2c, f). The schlieren are interpreted to have originated in the paleosome and then to have become variably entrained in, and later disaggregated by, the melt.

### Petrography

Detailed petrographic observations were made on all samples by optical microscopy and CL imaging in order to create a systematic framework for classifying kyanite petrogenesis. Thin sections for optical petrography were made from each of the samples. All other analyses were carried out on 100  $\mu\text{m}$  thick polished sections to preserve textural context. Greyscale panchromatic CL images were

taken using a FEI Quanta 200 3D FIB-SEM equipped with a Centaurus Cathodoluminescence Detector at The Open University, using a working distance of  $\sim 13$  mm and either 3.3 nA and 10 kV or 1.0 nA and 15 kV. Contrast and brightness settings were optimised for each analytical session, with the aim of highlighting internal variations in kyanite and reducing image noise. Where kyanite was in contact with strongly luminescent feldspars, brightness was reduced to stop excess feldspar luminescence affecting and washing out the kyanite luminescence. After acquisition, image brightness was adjusted manually using Adobe Photoshop. For large grains individual CL images were manually stitched together in Adobe Photoshop.

## Thin section descriptions

The sampled migmatites comprise metapelitic schists (paleosome) composed of biotite + muscovite + quartz + plagioclase + kyanite ± garnet ± tourmaline (Table 1), with leucosomes of quartz + plagioclase + K-feldspar + muscovite + kyanite that commonly host schlieren of biotite ± garnet. A summary of the main petrographic features of the samples is below; full sample descriptions can be found in the Online Resource S1. Samples with names ending in -x denote samples taken from float samples, generally from small stream valleys that suggest transport of material is minimal. Samples ending in -i or -ii indicate where multiple thin sections were cut from the same part of the hand sample. The sample ending in \_3 indicates it is one of multiple sections taken from different parts of the same large sample.

SPB-021x comprises a kyanite + garnet paleosome that is generally in sharp contact with a leucosome that contains kyanite-biotite + garnet schlieren. Garnet and biotite rims are typically chloritised. Muscovite is not abundant in the paleosome, but is present as both primary laths and as large grains surrounding kyanite in the leucosome. SPB-026bx has a similar mineralogy and migmatite style, with the addition of rare staurolite preserved in the schist near garnet grains, and fine trails of sillimanite at the margins of feldspar porphyroblasts in the leucosome.

SPB-023\_3 has a distinctive kyanite + biotite ± garnet ± tourmaline restite that is well segregated from the leucosome, which is kyanite-bearing. Tourmaline is up to 1 cm long in the restite but commonly only a few mm long in the leucosome. Muscovite is common in both the restite and the leucosome; it is typically skeletal and associated with quartz intergrowths where in contact with plagioclase. Centimetre-sized K-feldspar porphyroblasts dominate the leucosome.

SPB-031 is comprised of a kyanite + garnet paleosome with discontinuous patches of leucosome that are in sharp contact with the paleosome. Strongly deformed kyanite grains with kink bands are common throughout the paleosome and leucosome of this sample. Garnet is not present in the analysed thin sections of this sample, though it was observed locally in the field. Muscovite is uncommon in both the paleosome and leucosome but where present, appears in textural equilibrium with surrounding phases.

SPB-033 was collected from a heterogeneous outcrop that exposed patches of well-segregated boudinaged granitic lenses with no kyanite present, varying to patches containing stubby kyanite grains and patches of rock with a higher proportion of leucocratic material. In thin section, the contact between the leucosome and paleosome is diffuse, and biotite and garnet-rich schlieren are common in the leucosome. Quartz and kyanite are commonly significantly deformed. Muscovite is commonly intergrown with biotite.

SPB-035x, -036x and 037x all have similar mineralogy, with kyanite + garnet + tourmaline present in the paleosome. Sillimanite and rare staurolite is present in the paleosomes of SPB-035x. SPB-035x and SPB-036x both preserve sharp contacts between paleosome and leucosome. In both samples, the leucosomes contain kyanite and preserve schlieren and muscovite laths (with significantly higher proportion of muscovite to biotite in 35x). In sample SPB-037x, the leucosome–paleosome contact is much more diffuse and the spatial distribution of paleosome, leucosome and schlieren is more heterogeneous.

SPB-049i is from an outcrop where there is considerable compositional variability from psammitic kyanite-poor gneisses that show no evidence of melting to more pelitic kyanite schists containing folded leucosomes. Both samples are garnet-free. Biotite is typically disaggregated and distributed throughout the thin sections; however, some diffuse paleosome–leucosome contacts are present in other samples from the same outcrop. Muscovite is less abundant than biotite in the paleosome, and is present in leucosomes only as coarse cm-sized patches surrounding corroded kyanite.

## Kyanite morphology

Four different morphological types of kyanite are present in the studied samples: tabular (some of which are deformed), poikiloblastic, corroded, and prismatic. These morphological types are present in different microstructural positions, i.e. in the paleosome or the leucosome (Table 2). Multiple types of kyanite commonly coexist within a single sample, but not all samples contain all kyanite types (Table 2). There is no apparent link between type of kyanite and amount of leucosome present.

**Table 2** Petrogenetic kyanite classification based on microstructural position, kyanite morphology and CL zonation observed in E Bhutan migmatite samples

| Growth mechanism         | Sub-solidus            |           | Peritectic     | Magmatic                          |             |
|--------------------------|------------------------|-----------|----------------|-----------------------------------|-------------|
|                          | Paleosome              | Leucosome |                | Leucosome                         | Leucosome   |
| Microstructural position |                        |           | Leucosome      |                                   |             |
| Kyanite morphology       | Tabular                |           | Poikiloblastic | Poikiloblastic and tabular (rims) | Prismatic   |
| CL zoning                | Complex, sector zoning |           | Highly complex | Uniform                           |             |
| Grain part               | Core                   |           | Core           | Rim                               | Whole grain |

Large (0.1 to > 2 cm), *tabular*, stable kyanite crystals with no evidence of resorption or alteration at the crystal edges are common in the paleosome and leucosome regions of nearly all samples (Fig. 3a). In the paleosome, kink bands in kyanite and bent grains suggest post-growth deformation.

*Poikiloblastic* kyanite crystals, commonly 1–4 mm in size and present in clusters, contain abundant 0.1–1 mm inclusions of rutile and quartz (Fig. 3b) and are associated with cusped quartz lenses along their grain boundaries. Poikiloblastic grains are primarily found in sample SPB-049i and are only found in leucosome domains.

*Corroded*, ragged, kyanite grains are commonly (and exclusively) present in the leucosomes of most samples (not in SPB-023, SPB-026bx and SPB-031x), and are generally surrounded by large single grains of muscovite (Fig. 3c). These grains appear to originally have been of a similar size and shape to the tabular kyanite grains in the schists.

Thin *prismatic* crystals, 1–2 mm in length, are only associated with leucosome domains, primarily in samples SPB-021x and SPB-021xii (Fig. 3d).

### Zoning patterns (CL)

Four distinct zoning patterns (complex, sector, CL-bright, and uniform) were recognised in the cores and rims of the different morphologies of kyanite within CL images. Core and rim regions are commonly delineated by abrupt changes in CL intensity.

All tabular grains in the paleosomes are characterised by discontinuous patches of complex, streaky, and patchy CL responses (Fig. 4a). The cores of corroded kyanite grains have similar complex CL zonation (Fig. 4c), and sector zoning is distinguishable in some grains (Fig. 4c, d).

The poikiloblastic kyanite grains record complex internal zoning, characterised by bright and dark patches (commonly discontinuous) and ‘streaky’ zonation across the grains (Fig. 4b). Discrete patches are present within (what appear

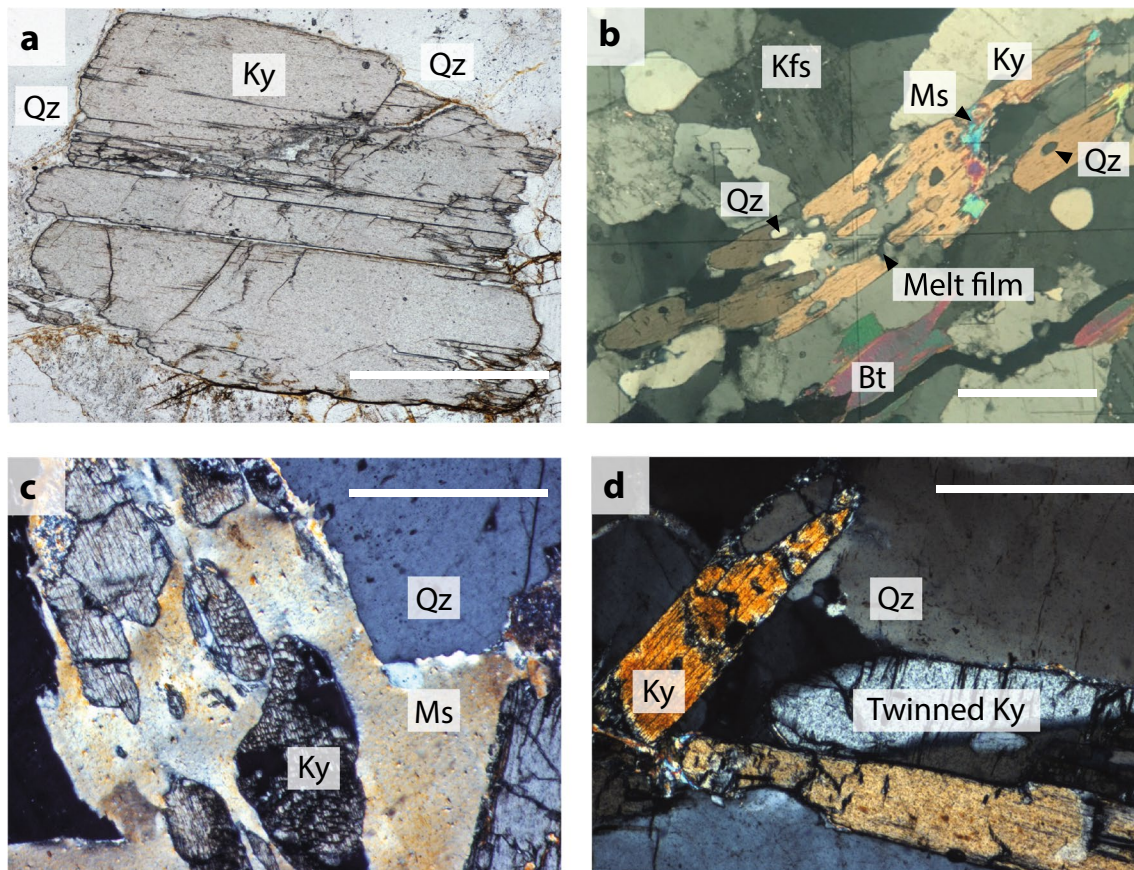


**Fig. 3** Photomicrographs of different morphological kyanite types. White scale bars are 500  $\mu\text{m}$ . **a** Tabular kyanite from paleosome of SPB-021x (plane polarised light). **b** Poikiloblastic kyanite with rutile and quartz inclusions in leucosome of SPB-049i (crossed polarised

light). Melt films are composed of quartz. **c** Corroded kyanite surrounded by muscovite in leucosome of SPB-021x (crossed polarised light). **d** Thin elongate kyanite in leucosome of SPB-021xii (crossed polarised light)



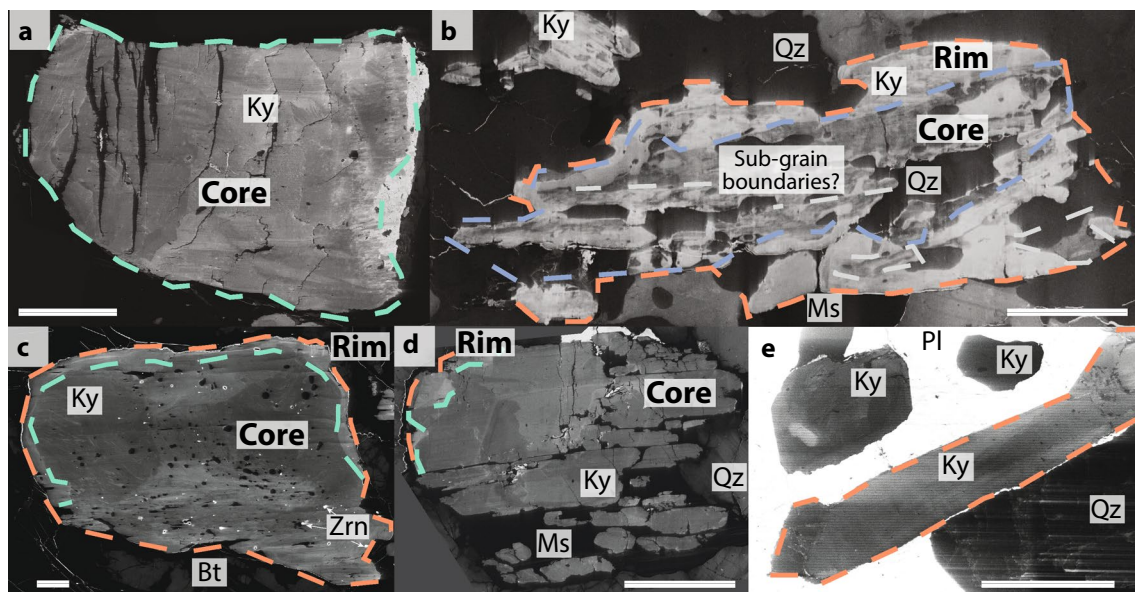


**Fig. 4** Representative cathodoluminescence (CL) images of observed kyanite zoning patterns. Colours of dashed lines indicate zones related to different petrogenetic types: green = sub-solidus, blue = peritectic, orange = magmatic. Scale bars 500  $\mu\text{m}$ . **a** Complex CL patterns in the core of tabular kyanite grain Ky08 from the paleosome of SPB-021x. Bright margin on the left side of this grain is an artefact of imaging and is not a grain rim. **b** Complex CL patterns in a poikiloblastic kyanite core surrounded by a CL-bright rim in grain Ky12 from the leucosome of SPB-049i. Potential sub-grain bounda-

ries are shown in grey dashed lines. **c** Complex CL patterns in a tabular kyanite core with sector zonation, surrounded by a CL-bright rim in grain Ky01 in the leucosome of SPB-023\_3. **d** Corroded kyanite grain Ky02 in the leucosome of sample SPB-021x showing complex CL patterns with faint sector zonation in the grain core surrounded by a CL-bright rim, both of which are truncated by ragged grain margin. **e** Thin prismatic kyanite grain Ky06 showing plain CL patterns, in the leucosome of SPB-021xii

to be) the same crystal, possibly indicating the presence of sub-grain domains within the larger kyanite grain (examples can be seen in Fig. 4b but are more visible in other grains).

Uniform CL-bright (and very rarely CL-dark) rims commonly surround tabular, poikiloblastic, and corroded kyanite grains in the leucosome. Rims on poikiloblastic grains are commonly discontinuous (Fig. 4b). The core–rim boundary in tabular grains generally mirrors that of the outer crystal shape (Fig. 4c); whereas in corroded grains, the core–rim boundary is commonly truncated by the irregular edge of the crystal (Fig. 4d). Bright kyanite rims and corroded kyanite grains are only found in the leucosomes.

The prismatic kyanite found in the leucosome records a uniform CL response with muted darker and lighter patches, with similar response to the uniform rims on the tabular and poikiloblastic grains (Fig. 4e).

### Kyanite petrogenesis classification

The petrographic and CL response observations together provide sufficient evidence to make preliminary interpretations of kyanite petrogenesis in these samples. As outlined in the introduction, kyanite may form by growth in the solid state ('sub-solidus'), as peritectic products of incongruent melting ('peritectic') or may form during melt crystallisation

('magmatic'). Table 3 outlines the petrographic observations that allow these different petrogenetic types to be differentiated.

Tabular kyanite with complex internal CL zoning is the only type of kyanite observed in the migmatite paleosomes (Fig. 4a). This type of kyanite is also present in some of the leucosomes, forming grain cores commonly surrounded by CL-bright rims (Fig. 4c). We therefore interpret these tabular grains or grain cores as forming under sub-solidus conditions; their presence in the leucosome suggests inheritance of sub-solidus kyanite from the paleosome/host rock by entrainment in the melt.

Poikiloblastic kyanite grains that are predominant in the leucosomes of sample SPB-049i contain plentiful inclusions of quartz (Fig. 4b). Since quartz is a reactant in both muscovite melting reactions (1) and (2), these inclusions suggest a peritectic origin for the poikiloblastic kyanite (peritectic crystals typically contain inclusions of the reactants from which they form, Cesare et al. 2015; Dyck et al. 2020; Erdmann et al. 2012). Furthermore, cusped quartz lenses along poikiloblastic kyanite grain boundaries (Fig. 3b) may be pseudomorphs after melt (Holness and Sawyer 2008; Holness et al. 2011; Sawyer 1999; Vernon 2011). This observation further suggests that poikiloblastic kyanite formed while

melt was present but before the melt crystallised, consistent with a peritectic origin.

When present, rims on the tabular and poikiloblastic cores are typically concentric and show bright CL responses (Fig. 4b, c). Their simple CL pattern and euhedral crystal shape suggest free growth in the presence of melt. As these rims are only associated with kyanite in the leucosomes, we interpret these to be magmatic rims representing syntaxial growth of kyanite during melt crystallisation (Hanchar and Miller 1993).

In many samples, kyanite grains are corroded. The corroded margins truncate the core–rim boundaries observable in the CL images. These grains are generally surrounded by single large, optically continuous grains of muscovite (Figs. 3c and 4d). Their ragged morphology suggests that after crystallisation of the rim on the sub-solidus core, the newly formed kyanite subsequently partly dissolved into the melt.

The thin prismatic kyanite crystals (Fig. 4e) also show a bright, uniform CL response that is similar to the response of the magmatic rims on tabular and poikiloblastic cores. These grains are only found in leucosomes. Prismatic grains are therefore interpreted to have wholly crystallised from the melt.

In summary, the petrographic observations made through optical microscopy and CL imaging allow three kyanite growth types to be clearly distinguished: sub-solidus, peritectic, and magmatic. Kyanite grains in many of the Bhutan migmatite samples record multiple episodes of growth and dissolution under different conditions, creating complex grains that require careful investigation to unravel their petrogenetic histories.

## Geochemistry

### Major element analyses

Major element concentrations were measured on carbon-coated thick sections using the Cameca SX100 microprobe equipped with 5 wavelength dispersive spectrometers at The Open University. Each spectrometer was routinely calibrated and verified during each analytical session using a selection of in-house standards. Major element reproducibility was ensured by analysis of an in-house secondary standard (Open University Garnet “NGA”) at the start of each session and compared to long-term trends (data collected for > 10 years). Spectrometers used for the following elements were: PET–K, P, Ca, Ti, LIF–Fe, TAP–Si, Mg, Na, Al. Major element analyses were carried out using a standard silicate analysis setup of 20 nA beam, 20 kV accelerating current and 10  $\mu$ m

beam size, at a working distance ~ 15 mm. The following oxides were measured: SiO<sub>2</sub>, TiO<sub>2</sub>, Al<sub>2</sub>O<sub>3</sub>, FeO, MgO, CaO, Na<sub>2</sub>O, K<sub>2</sub>O, P<sub>2</sub>O<sub>5</sub>, and MnO. Analyses were discarded if oxide totals for kyanite were < 99%.

### Trace element spot analyses

Spot analyses of <sup>24</sup>Mg, <sup>27</sup>Al, <sup>29</sup>Si, <sup>39</sup>K, <sup>43</sup>Ca, <sup>45</sup>Sc, <sup>49</sup>Ti, <sup>51</sup>V, <sup>53</sup>Cr, <sup>55</sup>Mn, <sup>56</sup>Fe, <sup>60</sup>Ni, <sup>65</sup>Cu, <sup>66</sup>Zn, <sup>71</sup>Ga, <sup>74</sup>Ge, <sup>90</sup>Zr, and <sup>137</sup>Ba were collected using a Photon Machines Analyte G2 193 nm excimer laser system, equipped with a HeLEX II laser ablation cell coupled to an Agilent 8800 Triple Quadrupole ICP-MS at The Open University.

ICP-MS tuning was carried out on the NIST SRM 612 glass with a 50  $\mu$ m spot, 10 Hz, 3.63 J/cm<sup>2</sup>. Analyses were run using a fluence of 2.5 J/cm<sup>2</sup>, a repetition rate of 10 Hz, and a 50  $\mu$ m spot size. Sample analysis lasted 30 s, with 30 s background measurement before the laser fired, and 40 s washout. Two analyses each of the NIST 612 and BCR-2G standards bracketed every 20 unknowns.

Data reduction was carried out using Iolite software (Paton et al. 2011). BCR-2G was used as the primary standard for Mg, Ca, Ti, Mn and Fe. NIST SRM 612 was used as the primary standard and BCR-2G as the secondary standard for all other elements. <sup>29</sup>Si was used as the internal standardisation element using values either from microprobe analyses carried out adjacent to LA-ICP-MS spots, or average SiO<sub>2</sub> concentrations measured by microprobe for each individual kyanite grain.

In order to assess data accuracy and precision, BCR-2G analyses were compared to published values (Jenner and O’Neill 2012) and long-term laboratory averages (Online Resource S2). Trace/major element concentrations measured by LA-ICP-MS maps/spots and electron microprobe were also compared for consistency (Online Resource S3).

### Trace element map acquisition

Kyanite in eight samples was mapped to reveal spatial changes in trace element concentrations. Quantitative maps of <sup>29</sup>Si (used as the internal standardising element), <sup>51</sup>V, <sup>53</sup>Cr and <sup>74</sup>Ge (chosen based on trends observed in spot analyses) were collected in thirteen kyanite grains using the LA-ICP-MS system at The Open University (as instrumentation described above). Maps were generated by moving the sample stage continuously underneath the laser beam with a fixed speed and spot size, allowing signals to be split into pixels from which compositional data can be extracted. The Teledyne Aerosol Rapid Introduction System (ARIS) was used to provide fast signal transport and washout rates allowing fast map acquisition. The He-carrier gas flow was tuned to produce optimal peak separation. Counting times were <sup>29</sup>Si = 0.003 ms,

$^{51}\text{V} = 0.0210$  ms,  $^{53}\text{Cr} = 0.0180$  ms and  $^{74}\text{Ge} = 0.0240$  ms, giving a total sweep time of 80 ms. Tuning was carried out using a laser beam masked into a  $10\ \mu\text{m}$  square at 50 Hz, a fluence of  $3.63\ \text{J}/\text{cm}^2$  and a fixed speed of  $30\ \mu\text{m}/\text{sec}$  on the NIST SRM 612 glass. Mapping was carried out using a  $10\ \mu\text{m}$  square at 150 Hz, a laser fluence of  $2.9\ \text{J}/\text{cm}^2$ , using a fixed dosage of either 12 or 15 shots per pixel and a scan speed of 125 or  $100\ \mu\text{m}/\text{sec}$  respectively. A  $20\ \mu\text{m}$  square spot size was used for mapping larger grains (e.g. SPB-049i\_Ky07, Online Resource Fig. S7.12). Parallel lines were positioned directly below the previous line (i.e.  $10\ \mu\text{m}$  below for  $10\ \mu\text{m}$  squares) using the same scanning direction (left to right) to ensure the same particle transport properties of each ablation. The NIST SRM 612 glass was used as a primary standard, by analysing four lines before and after each map. Grain scans took less than 4 h and thus, instrument drift was minimal and no correction was required.

Laser map data reduction was carried out using HDIP LA-ICP-MS imaging software (Teledyne Cetac). Quantification of count maps was carried out using  $^{29}\text{Si}$  as the internal standard element based on the average Si concentrations for each individual kyanite grain as measured by electron microprobe. Standardised data were then imported into XMapTools to facilitate the production of the final maps (Lanari et al. 2014). Raw Si counts were used to identify kyanite and masks were applied to LA-ICP-MS maps in order to exclude other phases analysed in the scan. A 2-pixel median filter was applied to all

exported map images to reduce noise but maintain visibility of textural features (see Lanari 2019). Whilst filtering may blur the sharpness of some interfaces, we do not deem this effect to be strong in our maps.

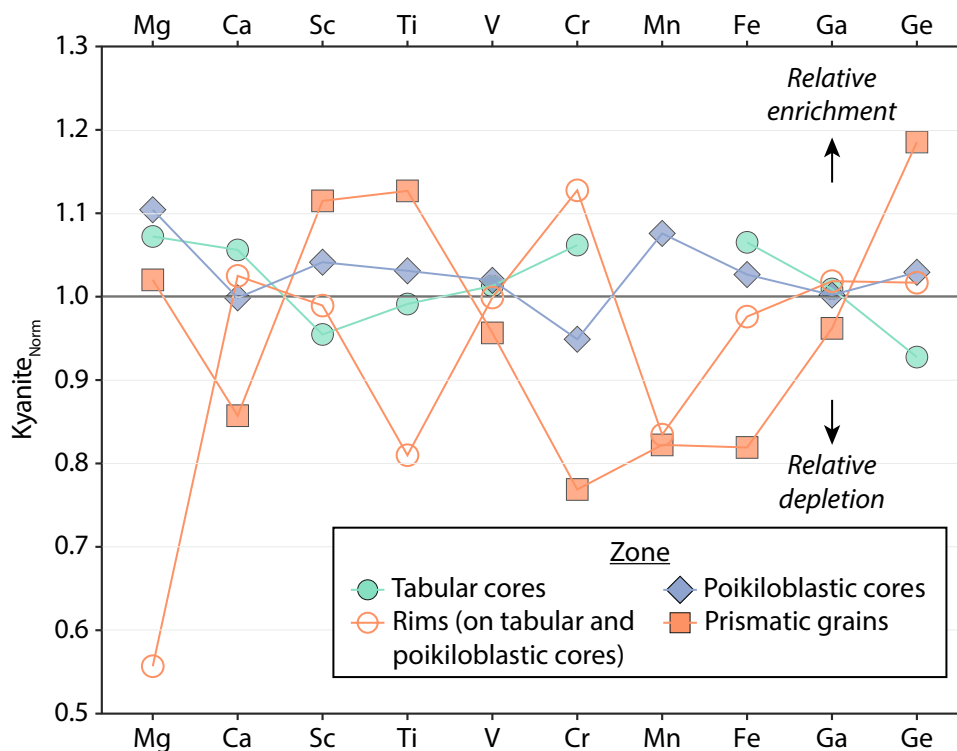
## Results

### Spot analyses

Trace element concentrations were measured in 227 spots in 63 kyanite grains from 10 samples, across all grain types and CL zones identified above. Full data tables are included in Online Resource S4. The variability in trace element concentrations by sample and across different textural zones is presented in Online Resource S5 and S6. Mg ( $\sim 17$ – $350$  ppm), Ti ( $\sim 7$ – $105$  ppm), V ( $\sim 20$ – $110$  ppm), Cr ( $\sim 3$ – $2850$  ppm), Fe ( $520$ – $6200$ ), Ga ( $\sim 19$ – $48$  ppm) and Ge ( $\sim 2$ – $17$  ppm) concentrations were above limits of detection in all grains. Ca ( $\sim 100$ – $1000$  ppm) and Sc ( $\sim 0.15$ – $4$  ppm) concentrations were mostly, but not always above limits of detection. 35 grains in all samples except SPB-031 and SPB-033, contained measurable amounts of Mn ( $\sim 0.26$ – $3$  ppm).

There is considerable variability in absolute trace element concentration between samples (see Online Resource S5). For example, kyanite in sample SPB-049i contains higher concentrations of Sc and Cr; kyanite in SPB-026bx, SPB-035xii and SPB-037x and SPB-049i contains higher concentrations of Fe. This sample-to-sample variation is

**Fig. 5** Average compositions of different kyanite zones, normalised to the average elemental composition of all kyanite in that sample

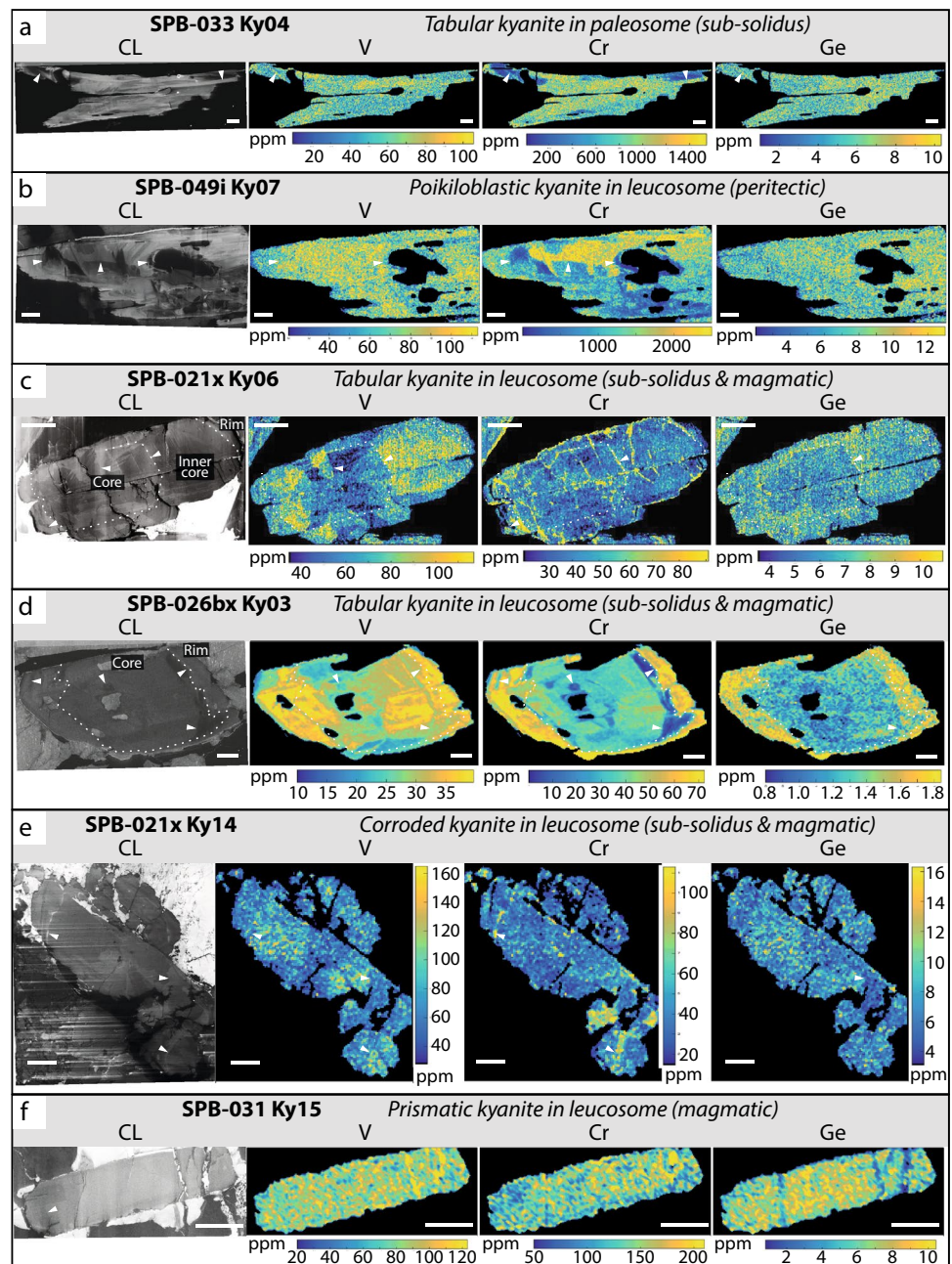


largely independent of kyanite petrogenesis. To filter out the effect of bulk enrichment or depletion across different samples, individual spot concentrations were normalised to the average concentration of that element in all of the kyanite (regardless of petrogenetic type) in that sample (Fig. 5). We recognise that concentrations are usually normalised to an average sample bulk rock concentration, but these samples are so modally, and therefore chemically, heterogeneous that a bulk average is less meaningful. Absolute concentrations (non-normalised values) for each kyanite and their petrogenetic type are presented in Online Resource S4 and

normalising values for each element in each sample are provided in Online Resource S7.

Sub-solidus tabular cores and peritectic poikiloblastic cores tend to have similar normalised values for all elements, and although there are subtle variations neither petrogenetic type shows any particular enrichment or depletion in any element. Magmatic rims (on both tabular and poikiloblastic cores) are strongly depleted in Mg, depleted in Ti and Mn, and relatively enriched in Cr. Magmatic prismatic grains are relatively depleted in Ca, Cr, Mn, and Fe, and enriched in Sc, Ti and Ge.

**Fig. 6** Comparison of zoning patterns visible in cathodoluminescence (CL) with LA-ICP-MS trace element maps of V, Cr and Ge. Scale bars are 200  $\mu\text{m}$ . Arrows denote features visible in the CL image that are also present in the LA-ICP-MS maps. LA-ICP-MS maps are created in XMapTools and use an auto-contrast scale, with concentrations in ppm, with a 2-median filter (see Lanari 2019)



## Trace element maps

Trace element maps showing key features for each petrogenetic type are shown in Fig. 6; all mapped grains are documented in Online Resource S8. Comparisons between LA-ICP-MS maps and individual spot analyses are provided in Online Resource S9 and demonstrate the good agreement in measured concentrations of V, Cr and Ge between map and spot analyses.

The maps show that absolute V, Cr and Ge concentrations vary considerably across individual kyanite grains in different samples and between the different petrogenetic types. Many features visible in the CL images are also present in the trace element maps, including both diffuse and abrupt zone boundaries. Not all the elemental maps display all features observed in CL. High Cr concentrations tend to correlate well with bright CL features (and vice versa). Changes in Cr concentrations tend to be sharp, as they are in CL, picking out fine-scale variations. Cracks in kyanite grains also tend to be high in Cr. Changes in V concentrations are generally more subtle and patchy but often also correspond to changes in CL intensity. Ge concentrations measured are typically low across all grains with little variation across the grain; where there is variation in concentrations this often relates to boundaries in CL and Cr or V concentrations changes.

Sub-solidus cores generally have low concentrations of all analysed trace elements relative to their rims (Fig. 6a, c, e). Complex patchy or streaky CL zoning patterns that characterise the sub-solidus tabular cores do not clearly correspond to elemental zoning patterns (Fig. 6a, c). The sector zoning visible in the CL images (especially in the core of SPB-021 × Ky06) is distinctly highlighted by V concentrations (Fig. 6c).

Peritectic poikiloblastic kyanite core maps show similar features to the sub-solidus cores, with patchy CL response and patchy trace element zoning being common. Strong variations in Cr concentrations correspond well to some of the rounded sub-domains identifiable in the CL images, but these domains do not directly match changes in V or Ge concentrations (Fig. 6b).

Magmatic rims are characterised by brighter CL responses, which strongly matches elevated concentrations of Cr, and to a lesser degree, Ge (Fig. 6d). Discontinuous rims showing narrow bright lines in CL are also visible in Cr concentration maps (Fig. 6e). The rim region in kyanite grain SPB-021 × Ky06 (Fig. 6c) and SPB-026bx Ky03 (Fig. 6d) shows pseudo-oscillatory zonation, with dark CL zones that correspond to Cr-poor regions.

Magmatic prismatic grains (Fig. 6f) show very little variation in CL response. The corresponding V, Cr and Ge maps do show some variation but do not show any clear features. This does not appear to be due to lower concentrations of

V, Cr or Ge, as SPB-031x Ky15 has higher concentrations of these elements versus other grains that do show strong variations.

As both Cr and V element maps match well to changes in intensity in CL images, maps of Cr/V were computed in XMapTools (Lanari 2019; Lanari et al. 2014) (Fig. 7a, c, e). These maps show excellent correlation with the textural features observed in their corresponding CL images (Fig. 7b, d, f). In general, a bright CL response corresponds to high Cr/V. Cr/V tends to vary between 0 and 3, but extreme ratios (up to 19) are recorded in kyanite grains SPB-033x Ky04 (Fig. 7a), linked to variability in Cr concentrations (SPB-033x Ky04 maximum Cr = ~ 1400 ppm versus < 200 ppm in other samples).

## Discussion

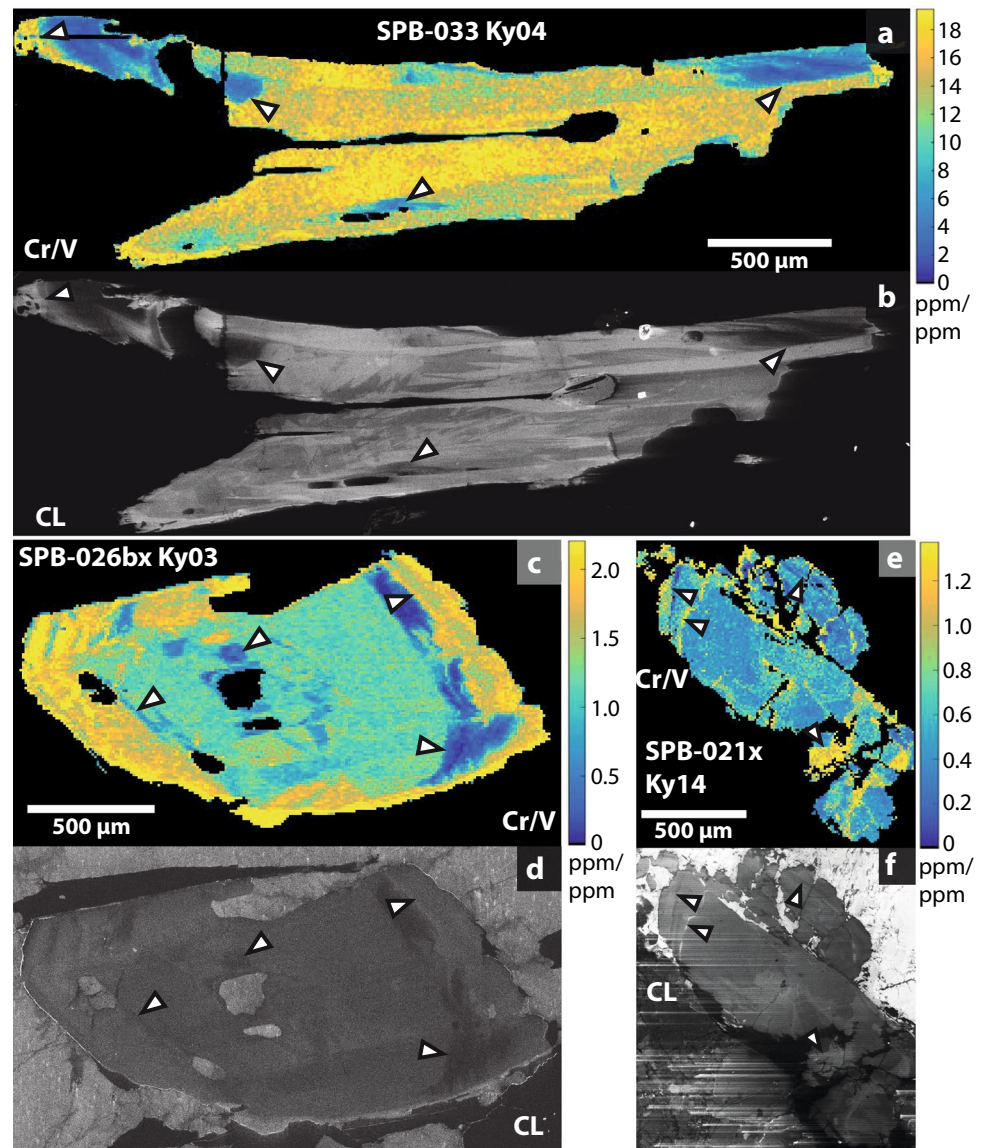
The geochemical data support the evidence from the petrographic and CL observations that kyanite in the Bhutan migmatites grew in three different environments (in the solid state, as a peritectic product during melting, and crystallising directly from melt). All three datasets offer complementary and supplementary insights into kyanite petrogenesis that could be applied to other orogenic belts to provide insight into the conditions and evolution of partial melting processes.

### Protolith control on trace element concentrations in kyanite

Kyanite grains from different locations in East Bhutan show distinctive trace element compositions, (Online Resources Fig. S5.1); for example, kyanite in samples from Buyong (SPB-049i) has higher concentrations of Fe, Cr and Sc compared to other localities. This variation is largely independent of kyanite petrogenesis; for example, analyses of kyanite from Tangmachu (SPB-026bx) and Rongthung (SPB-035x, -036x, -037x), include both sub-solidus and melt-crystallised kyanite but kyanite grains from these locations are all still significantly higher in Fe. This suggests that bulk protolith composition controls abundances of trace elements in kyanite, at least for Fe, Cr and Sc.

It has previously been suggested that V and Cr concentrations in kyanite are strongly controlled by the protolith composition, with distinctive compositional differences between kyanites formed in metasedimentary vs. metabasaltic rocks (Müller et al. 2016). All samples analysed in this study are from the structurally lower portions of the GHS unit in Bhutan (Fig. 1), which is composed of pelitic and psammitic schists, i.e. sedimentary/felsic in the classification

**Fig. 7** Selected LA-ICP-MS maps of Cr/V compared to CL images of the same grains. Arrows denote textural features that are observed in both. Bright streaks from bright areas into darker areas in the CL images are artefacts of nearby high-intensity phases and poorly polished surfaces



of Müller et al. (2016). The V and Cr concentrations in our metasedimentary samples plot across all the fields delineated by the Müller et al. (2016) dataset (Fig. 8), not just the sedimentary field, suggesting that these elements may not provide useful source discriminators of the protolith, at least not in the Himalaya.

### Link between CL response and geochemistry

Chromium and Ti are known to be CL activators in kyanite, whereas Fe is a known CL quencher (Gaft et al. 2015; Habermann 2002; Pagel et al. 2000; Wojtowicz 1991), and variations in these elements have been shown to correlate well with changes in CL intensity (Müller et al. 2003). Vanadium is not a known activator (Ramseyer and Mullis 2000),

though it has been suggested as a luminescent centre in synthetic materials (Gaft et al. 2015).

Non-systematic relationships between trace element composition and CL zoning patterns in kyanite have previously been documented (Horkley et al. 2013; Kendrick and Indares 2017; Müller et al. 2016; Peterman et al. 2021). The trends of high Cr corresponding to bright CL, and high-Ti corresponding to blue CL emissions reported in some studies (Müller et al. 2016) are not observed in others (Peterman et al. 2021). Elements such as Mg, Fe, Ti, and P are thought to exert a control over CL response depending on their concentrations, but CL intensity alone cannot be used to identify areas of enrichment or depletion in any element alone (Peterman et al. 2021). Similarly we see no clear correlation between LA-ICP-MS spot analyses and CL intensity.

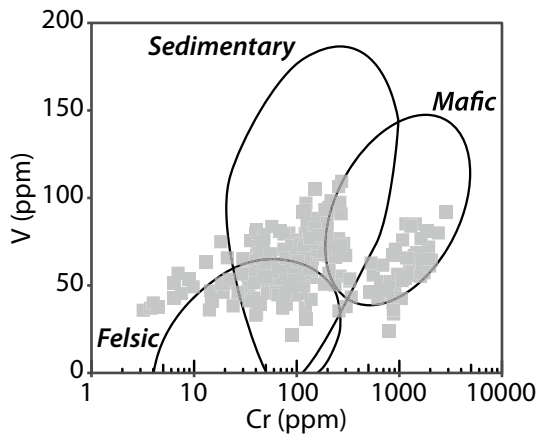


**Fig. 8** Vanadium versus Cr concentrations in E Bhutan kyanite grains (grey squares). Black ellipses represent the distinctions in kyanite compositions in felsic, sedimentary, and mafic source rocks suggested by the Müller et al. (2016) dataset

The trace element maps show that there is some systematic correlation between CL response and the concentrations of V, Cr and Ge, though this relationship is not clear for any single element. The strongest correlation occurs between CL intensity and Cr/V (Fig. 7). Vanadium concentrations document the sector zoning patterns in the kyanite cores well, with darker sectors recording higher V concentrations. Where CL responses are bright, as in rims, patches and margins in grain interiors, these match well to high concentrations of Cr, and vice versa.

Cr variations tend to pick out more detailed features than V element maps, which are patchier. Germanium concentrations broadly follow the larger contrasts in CL zoning (and therefore Cr and V concentrations), but resolution in the Ge maps may be limited due to low concentrations (Ge is typically < 10 ppm). More work is required to understand both the variability in trace element geochemistry in kyanite as well as its link to CL response, but it is clear, particularly from Cr/V maps, that kyanite grains are able to record changing geochemical conditions as they grow.

**Indicators of petrogenesis**

Three petrogenetic origins of kyanite have been suggested from petrographic observations and CL imagery: sub-solidus growth, peritectic growth and growth during melt crystallisation. These observations are summarised in Fig. 9.

Cores of many kyanite grains present in migmatite leucosomes have similar CL zoning patterns and normalised trace element concentrations to tabular sub-solidus grains present in paleosomes. These observations suggest entrainment or “inheritance” of sub-solidus kyanite grains into the melt.

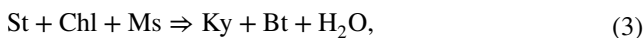
Complex internal CL zoning patterns similar to those observed in the sub-solidus (tabular) and peritectic (poikiloblastic) kyanite cores have previously been suggested as representing “chemomorphs” of previous phases (Horkley et al. 2013). The geochemical data support this suggestion,

**Fig. 9** Summary of observations of the different kyanite petrogenetic types observed in E Bhutan migmatites and their key geochemical indicators. Arrows represent relative enrichment or depletion in that element

| Growth mechanism                     | Sub-solidus  |           | Peritectic     | Melt crystallised               |                            |
|--------------------------------------|--|-----------|----------------|---------------------------------|----------------------------|
|                                      | Microstructural position   | Paleosome | Leucosome      | Leucosome                       | Leucosome                  |
| Kyanite Morphology                   | Tabular  |           | Poikiloblastic | Poikiloblastic & tabular (rims) | Prismatic                  |
| CL zoning                            | Complex, sector zoning   |           | Highly complex | Uniform                         |                            |
| Grain domain                         | Core   |           | Core           | Rim                             | Whole grain                |
| Schematic evolution of microtextures |  |           |                |                                 |                            |
| Geochemical evidence                 | Similar concentrations, regardless of microstructural position, reflecting protolith composition |           |                | ↑Cr<br>↓Mg, Mn, Ti              | ↑Sc, Ti<br>↓Mn, Cr, Fe, Ge |

with large absolute and normalised ranges in trace element concentrations being recorded in these zones.

The sector zoning apparent in the CL images of sub-solidus kyanite in SPB-021x is also observed in the V element map of the same grain (Fig. 6c). Similar sector zoning recorded in Fe, P, Mg and Ti concentrations measured by EPMA has been described in kyanite by Peterman et al. (2021). Though not widespread in the sub-solidus kyanite in this study, this sector zoning could indicate the growth of kyanite at the expense of staurolite. Sector zoning is a phenomenon long recorded in staurolite from many orogenic belts (Hollister 1970) and the crystallographic similarity of kyanite and staurolite could enable kyanite to inherit a zoning pattern from staurolite (Horkley et al. 2013). Staurolite is also a common precursor to kyanite in metamorphic rocks and there are a number of staurolite-out reactions that have been linked to kyanite growth for aluminous pelites, including but not limited to;



(Daniel et al. 2003; Yang and Rivers 2001). There is no textural evidence to indicate reaction between staurolite and kyanite in our samples, though relicts of irregular staurolite exist in samples SPB-026bx and SPB-035x adjacent to garnet. The lack of direct textural relationship between staurolite and kyanite has previously been noted in the literature, even where their coexistence is more petrographically obvious (Pattison and Spear 2018). There is also no clear textural evidence in these migmatites for or against garnet growth coeval with kyanite growth or staurolite breakdown.

Poikiloblastic kyanite is interpreted to form peritectically during melt-forming reactions. CL imagery suggests that clusters of poikiloblastic grains formed by grain coalescence during growth. Coalescence may provide an explanation for the geochemical diversity of this type of kyanite. The chemical zoning in individual grains or sub-grains may also have later been further modified by diffusive re-equilibrium (Erdmann et al. 2012). This may explain why zoning in poikiloblastic cores appears strongest in the Cr element maps, whereas the zoning in the V and Ge maps is more diffuse (Fig. 6b). Due to a lack of diffusion data for trace elements in kyanite, we can neither exclude nor confirm the possibility that the complex CL textures in the poikiloblastic kyanite are a result of diffusive re-equilibrium.

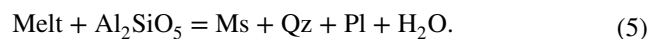
CL-bright (uniform) syntaxial rims and prismatic grains (magmatic grains) have been interpreted as having grown in the melt. These grains and zones show more uniform trace element patterns compared with the sub-solidus and peritectic grains, as well as being strongly enriched in Cr and depleted in Mg and Ti and Mn. Prismatic grains are

also depleted in Mn, as well as Cr and Fe, and are relatively enriched in Sc, Ti and Ge. Although interpreted to have crystallised from melt in a similar manner to the rims on other kyanite types, prismatic grains have different and highly variable normalised compositions; this elemental variability is invisible in CL response.

It is likely that local differences in nucleation kinetics within individual migmatites are responsible for the two different types of magmatic kyanite growth, with rims able to form epitaxially on existing kyanite grains, and prismatic grains nucleating independently. The implication is, therefore, that these grains will be crystallising from the melt at different times, or in different domains in the melt, meaning that they are subject to the changing conditions of the melt as other phases crystallise. Phases such as muscovite and potentially garnet crystallising from the melt (evidence for the latter is unclear in these samples, however) can both accommodate the same trace elements as those incorporated into kyanite, and will therefore also exert a control over the trace element budget of co-crystallising phases. This may explain the significant geochemical variability of the magmatic kyanite in these migmatites, but quantification of this is beyond the scope of this study.

## Implications for melt formation

Partial melting of aluminous pelitic protoliths generates Al-rich melts that are capable of crystallising an aluminosilicate on cooling (Zen 1988). Our samples show numerous examples of different petrogenetic types of kyanite in close proximity to each other. For example, prismatic magmatic kyanite grains in sample SPB-021xii occur within centimetres of magmatic-rimmed tabular kyanite and corroded kyanite grains. The muscovite surrounding the corroded kyanite grains suggests a change in the P-T-a(H<sub>2</sub>O) conditions such that the kyanite is no longer in equilibrium with the melt. Such a change could lead to kyanite back-reacting with the melt in a reversal of the muscovite-dehydration reaction (Kriegsman 2001);



The presence of grains of kyanite recording different petrogenetic histories in close proximity to each other suggests very localised variations in geochemical environments and disequilibrium on a local scale.

The scarcity of muscovite in the paleosomes of the studied migmatites implies that muscovite has been consumed in muscovite dehydration reactions that produced melt (reactions (1) and (2)), consistent with previous studies of GHS rocks (Harris et al. 1995). Both of these reactions produce peritectic kyanite, yet peritectic kyanite is recognised in only one of the sampled migmatites. This apparent scarcity could



be due to a lack of preservation of peritectic kyanite; as it will be generated simultaneously with melt, grain boundaries are likely to be in contact with melt, which means there is a high potential for back-reaction between melt and kyanite during cooling. However, unlike the back-reaction described above associated with corroded kyanite, muscovite is not found surrounding peritectic kyanite, nor does peritectic kyanite appear corroded. It is likely, therefore, that the apparent scarcity of peritectic kyanite is the result of our small sample set that is not necessarily representative of the regional distribution of kyanite across the Himalayan orogen.

It is also possible that the peritectic kyanite formed as a result of dehydration melting of biotite, which would occur at higher temperatures after muscovite has been consumed (Vielzeuf and Holloway 1988)



Biotite dehydration melting, where reactant biotite composition allows, could also cause the resorption of peritectic kyanite formed previously by muscovite dehydration, and thus may explain the lack of peritectic kyanite in the studied samples. There is, however, abundant biotite in both the leucosome and paleosome of all studied samples and there is no textural evidence for the breakdown of biotite to form melt. The low volumes of leucosome observed in the field also indicate that little melt was produced, which also suggests that any biotite dehydration melting was limited. We, therefore, favour the muscovite dehydration melting reaction(s) (1) or (2) as providing the dominant mechanism for melt (and peritectic kyanite) production in the studied samples.

The presence of water, as well as controlling the melt-forming reaction and thus what type of kyanite is produced, will also affect the volume of melt produced and the temperature at which melting can occur. At low temperatures, fluid-present muscovite dehydration will produce low volumes of melt from fertile lithologies whenever fluid is available (reaction (1)). Fluid-present melting may, therefore, also explain the relative rarity of these kyanite migmatites throughout the GHS as a whole, and at an outcrop scale where small volume leucosomes are only found in the mica-rich schists.

### Implications for P–T determinations and Himalayan tectonics

As a key pressure indicator in metamorphic rocks, kyanite is useful for general P–T constraints. Most kyanite grains in our migmatite samples formed in multiple growth episodes by multiple different mechanisms. Caution is therefore needed when the presence of kyanite in migmatite leucosomes or granites is used to infer P–T constraints on the

conditions of melting. The majority of the kyanite cores in our migmatite samples formed under sub-solidus conditions and therefore place no constraints on the P–T conditions at which melt formed or crystallised. We can only infer melting in the kyanite stability field in samples where peritectic or magmatic kyanite has been identified.

In Eastern Bhutan, only samples SPB-021x, SPB-031, SPB-036x and SPB-049i provide evidence for kyanite that grew via peritectic reactions or during melt crystallisation. Migmatites in these areas therefore provide evidence for melt crystallisation in the kyanite field—interpreted as melting along the prograde metamorphic path. Such melts are implicated as key evidence for the “channel flow” model (Beaumont et al. 2001), whereby early melt-weakening of the GHS drove the change from burial to exhumation tectonics. Detailed geochronology is still required to determine exactly when the melt formed and hence to provide further tests of this model, and/or more recent composite tectonic models that consider that different tectonic processes can be occurring at different times within the GHS unit and across the Himalaya (Carosi et al. 2018). Testing these composite models in Bhutan is of particular importance as kyanite-bearing migmatites have been dated to form much earlier (18–16 Ma) (Daniel et al. 2003) here than elsewhere in the Himalaya (often older than 24 Ma: Groppo et al. 2010; Iaccarino et al. 2015; Imayama et al. 2012; King et al. 2011; Lee et al. 2004; Prince et al. 2001; Rubatto et al. 2013). Combining geochronology with detailed information on petrogenesis is required to produce the accurate P–T–t paths that are critical for the evaluation of tectonic models in the Himalaya and other ancient orogens.

## Conclusions

Kyanite grains in migmatites preserve evidence of growth through a variety of different mechanisms that may be distinguished by detailed petrographic observation, CL imaging and geochemical analysis. Trace element abundances do not, on their own, allow the recognition of specific petrographic type. However, the geochemical dataset provides complementary information that enriches the petrogenetic classification scheme based on petrographic observations and CL response.

Sub-solidus growth of kyanite is characterised by tabular-shaped grains or cores with complex internal zoning visible in CL. The zoning and variability of chemical compositions suggest growth via continuous metamorphic reactions and/or the inheritance of textures from previous phases such as staurolite. The presence of sub-solidus kyanite in the leucosome indicates entrainment of sub-solidus kyanite into the melt. Peritectic kyanite, identifiable by poikiloblastic

texture, also has complex internal zoning visible in CL, but is only found in the leucosome.

CL-bright rims on xenocrystic sub-solidus or peritectic kyanite cores that are enriched in Cr and depleted in Mg and Ti represent epitaxial kyanite growth on existing grains via crystallisation from the melt. Newly crystallised magmatic kyanite without complex core domains preserves simple CL zoning patterns. These grains show a depletion in Cr and enrichment in Sc, Ti and particularly Ge, in comparison to other petrogenetic types.

Overall, our datasets show that the presence of kyanite in granites or migmatite leucosomes does not necessarily imply that the kyanite grew in the presence of melt. The recognition of different petrogenetic mechanisms by which kyanite can grow, along with the recognition that a single grain of kyanite can preserve multiple different growth zones that are not subsequently resorbed or modified, has implications for the interpretation of kyanite-bearing granitic rocks and hence for constraining tectonic models of orogenesis.

**Supplementary Information** The online version contains supplementary material available at <https://doi.org/10.1007/s00410-022-01991-w>.

**Acknowledgements** Research was funded by the NERC CENTA Doctoral Training Partnership and a British Geological Survey CASE studentship awarded to Stacy E. Phillips (SEP). Thanks are given to Kinley, Tandin, Nyima, and the rest of the crew at Namsay Adventures for their fieldwork assistance in Bhutan. Michelle Higgins, Kay Knight, Giulia Degli Alessandrini, Sam Hammond, and Frances Jenner are thanked for their assistance in sample preparation and analysis. SEP thanks Eleni Wood for fruitful discussions throughout the project.

**Author contributions** TWA, CJW, and NBWH contributed to the study conception and design as part of SEP's PhD project. Sample collection, preparation, and analyses were performed by SEP. BEK provided substantial input into the trial and development of new LA-ICP-MS analysis routines. The manuscript was written by SEP with input from all co-authors.

**Funding** This study was funded by the NERC CENTA Doctoral Training Partnership and a British Geological Survey CASE studentship (GA/16S/013, NEE2152S BUFI) awarded to Stacy Phillips.

**Data availability** The online version of this article contains supplementary material, which is available to authorised users.

**Code availability** Not applicable.

## Declarations

**Conflict of interest** The authors declare that they have no conflict of interest.

**Open Access** This article is licensed under a Creative Commons Attribution 4.0 International License, which permits use, sharing, adaptation, distribution and reproduction in any medium or format, as long as you give appropriate credit to the original author(s) and the source, provide a link to the Creative Commons licence, and indicate if changes were made. The images or other third party material in this article are included in the article's Creative Commons licence, unless indicated otherwise in a credit line to the material. If material is not included in

the article's Creative Commons licence and your intended use is not permitted by statutory regulation or exceeds the permitted use, you will need to obtain permission directly from the copyright holder. To view a copy of this licence, visit <http://creativecommons.org/licenses/by/4.0/>.

## References

- Albee AL, Chodos AA (1969) Minor element content of coexistent  $\text{Al}_2\text{SiO}_5$  polymorphs. *Am J Sci* 267:310–316. <https://doi.org/10.2475/ajs.267.3.310>
- Beaumont C, Jamieson RA, Nguyen MH, Lee B (2001) Himalayan tectonics explained by extrusion of a low-viscosity crustal channel coupled to focused surface denudation. *Nature* 414:738–742. <https://doi.org/10.1038/414738a>
- Carosi R, Montomoli C, Langone A, Turina A, Cesare B, Iaccarino S, Fascioli L, Visonà D, Ronchi A, Rai SM (2015) Eocene partial melting recorded in peritectic garnets from kyanite-gneiss greater Himalayan sequence, Central Nepal. *Geol Soc London Spec Pubs* 412:111–129. <https://doi.org/10.1144/SP412.1>
- Carosi R, Montomoli C, Iaccarino S (2018) 20 years of geological mapping of the metamorphic core across central and eastern Himalayas. *Earth-Science Rev* 177:124–138. <https://doi.org/10.1016/j.earscirev.2017.11.006>
- Cesare B, Acosta-Vigil A, Bartoli O, Ferrero S (2015) What can we learn from melt inclusions in migmatites and granulites? *Lithos* 239:186–216. <https://doi.org/10.1016/j.lithos.2015.09.028>
- Chinner GA, Smith J, Knowles C (1969) Transition metal contents of  $\text{Al}_2\text{SiO}_5$  polymorphs. *Am J Sci* 267-A:96–113
- Cottle JM, Larson KP, Kellett DA (2015) How does the mid-crust accommodate deformation in large, hot collisional orogens? A review of recent research in the Himalayan orogen. *J Struct Geol* 78:119–133
- Daniel CG, Hollister LS, Parrish R, Grujic D (2003) Exhumation of the main central thrust from lower crustal depths, eastern Bhutan Himalaya. *J Metamorph Geol* 21:317–334. <https://doi.org/10.1046/j.1525-1314.2003.00445.x>
- Dasgupta S, Chakraborty S, Neogi S (2009) Petrology of an inverted Barrovian sequence of metapelites in Sikkim Himalaya, India: constraints on the tectonics of inversion. *Am J Sci* 309:43–84. <https://doi.org/10.2475/01.2009.02>
- Davidson C, Grujic D, Hollister LS, Schmid SM (1997) Metamorphic reactions related to decompression and synkinematic intrusion of leucogranite, high Himalayan crystallines, Bhutan. *J Metamorph Geol* 15:593–612. <https://doi.org/10.1111/j.1525-1314.1997.tb00638.x>
- Deer WA, Howie RA, Zussman J (2013) Kyanite. An Introduction to the Rock-Forming Minerals, 3rd edn. Mineralogical Society of Great Britain and Ireland, London, pp 498
- Dyck B, Waters DJ, St-Onge MR, Searle MP (2020) Muscovite dehydration melting: reaction mechanisms, microstructures, and implications for anatexis. *J Metamorph Geol* 38(1):29–52
- Erdmann S, Scaillet B, Kellett DA (2012) Textures of peritectic crystals as guides to reactive minerals in magmatic systems: new insights from melting experiments. *J Petrol* 53:2231–2258. <https://doi.org/10.1093/petrology/egs048>
- Gaft M, Reifeld R, Panczer G (2015) Minerals radiometric sorting and online process control. In: Modern luminescence spectroscopy of minerals and materials. Springer, Cham, pp 499–575
- George FR, Gaidies F, Boucher B (2018) Population-wide garnet growth zoning revealed by LA-ICP-MS mapping: implications for trace element equilibration and syn-kinematic deformation during crystallisation. *Contrib to Mineral Petrol* 173:74. <https://doi.org/10.1007/s00410-018-1503-0>

- Godin L, Parrish R, Brown RL, Hodges KV (2001) Crustal thickening leading to exhumation of the Himalayan metamorphic core of Central Nepal: insight from U-Pb geochronology and  $^{40}\text{Ar}/^{39}\text{Ar}$  thermochronology. *Tectonics* 20:729–747. <https://doi.org/10.1029/2000TC001204>
- Greenwood LV, Argles TW, Parrish RR, Harris NBW (2015) The geology and tectonics of central Bhutan. *J Geol Soc Lon.* <https://doi.org/10.1144/jgs2015-031>
- Groppo C, Rubatto D, Rolfo F, Lombardo B (2010) Early oligocene partial melting in the main central thrust zone (Arun valley, eastern Nepal Himalaya). *Lithos* 118:287–301. <https://doi.org/10.1016/j.lithos.2010.05.003>
- Grujic D, Hollister LS, Parrish RR (2002) Himalayan metamorphic sequence as an orogenic channel: Insight from Bhutan. *Earth Planet Sci Lett* 198:177–191. [https://doi.org/10.1016/S0012-821X\(02\)00482-X](https://doi.org/10.1016/S0012-821X(02)00482-X)
- Guilmette C, Indares A, Hébert R (2011) High-pressure anatectic paragneisses from the Namche Barwa, Eastern Himalayan Syntaxis: Textural evidence for partial melting, phase equilibria modeling and tectonic implications. *Lithos* 124:66–81. <https://doi.org/10.1016/j.lithos.2010.09.003>
- Habermann D (2002) Quantitative cathodoluminescence (CL) spectroscopy of minerals: possibilities and limitations. *Mineral Petrol* 76:247–259. <https://doi.org/10.1007/s007100200044>
- Hanchar JM, Miller CF (1993) Zircon zonation patterns as revealed by cathodoluminescence and backscattered electron images: Implications for interpretation of complex crustal histories. *Chem Geol* 110:1–13. [https://doi.org/10.1016/0009-2541\(93\)90244-D](https://doi.org/10.1016/0009-2541(93)90244-D)
- Harris NBW, Inger S (1992) Geochemical characteristics of pelite-derived granites. *Contrib Miner Petrol* 110:46–56
- Harris NBW, Massey J (1994) Decompression and anatexis of Himalayan metapelites. *Tectonics* 13:1537–1546. <https://doi.org/10.1029/94TC01611>
- Harris N, Ayres M, Massey J (1995) The geochemistry of granitic melts produced during the incongruent melting of muscovite: implications for the extraction of Himalayan leucogranite magmas. *J Geophys Res* 100:15767–15777
- Harris NBW, Caddick M, Košler J, Goswami S, Vance D, Tindle AG, Kosler J, Goswami S, Vance D, Tindle AG (2004) The pressure-temperature-time path of migmatites from the Sikkim Himalaya. *J Metamorph Geol* 22:249–264. <https://doi.org/10.1111/j.1525-1314.2004.00511.x>
- Harrison TM, Lovera OM, Grove M (1997) New insights into the origin of two contrasting Himalayan granite belts. *Geology* 25:899–902. [https://doi.org/10.1130/0091-7613\(1997\)025%3c0899:NII-TOO%3e2.3.CO;2](https://doi.org/10.1130/0091-7613(1997)025%3c0899:NII-TOO%3e2.3.CO;2)
- Harrison TM, Grove M, McKeegan KD, Coath CD, Lovera OM, Le Fort P (1999) Origin and episodic emplacement of the manaslu intrusive complex. *Central Himal J Petrol* 40:3–19. <https://doi.org/10.1093/ptro/40.1.3>
- Herz N, Dutra CV (1964) Geochemistry of some kyanites from Brazil. *Am Mineral* 49:1290–1305
- Hodges KV (2000) Tectonics of the Himalaya and southern Tibet from two perspectives. *GSA Bull* 112:324–350. [https://doi.org/10.1130/0016-7606\(2000\)112%3c324:TOTHAS%3e2.0.CO;2](https://doi.org/10.1130/0016-7606(2000)112%3c324:TOTHAS%3e2.0.CO;2)
- Hodges KV, Parrish R, Searle MP (1996) Tectonic evolution of the central Annapurna Range, Nepalese Himalayas. *Tectonics* 15:1264–1291. <https://doi.org/10.1029/96TC01791>
- Hollister LS (1970) Origin, mechanism, and consequences of compositional sector-zoning in staurolite. *Am Mineral* 55:742–766
- Holness MB, Sawyer EW (2008) On the pseudomorphing of melt-filled pores during the crystallization of migmatites. *J Petrol* 49:1343–1363. <https://doi.org/10.1093/ptrology/egn028>
- Holness MB, Cesare B, Sawyer EW (2011) Melted rocks under the microscope: microstructures and their interpretation. *Elements* 7:247–252. <https://doi.org/10.2113/gselements.7.4.247>
- Horkley LKS, Spear FS, Ruscitto DM, Tailby ND (2013) The secret life of kyanite. In: Geological Society of America Abstracts with Programs, vol 45, no 1, p 96
- Iaccarino S, Montomoli C, Carosi R et al (2015) Pressure-temperature-time-deformation path of kyanite-bearing migmatitic paragneiss in the Kali Gandaki valley (Central Nepal): investigation of late eocene-early oligocene melting processes. *Lithos* 231:103–121. <https://doi.org/10.1016/j.lithos.2015.06.005>
- Imayama T, Takeshita T, Yi K, Cho DL, Kitajima K, Tsutsumi Y, Kayama M, Nishido H, Okumura T, Yagi K, Itaya T, Sano Y (2012) Two-stage partial melting and contrasting cooling history within the higher Himalayan crystalline sequence in the far-eastern Nepal Himalaya. *Lithos* 134–135:1–22. <https://doi.org/10.1016/j.lithos.2011.12.004>
- Jenner FE, O'Neill HSC (2012) Major and trace analysis of basaltic glasses by laser-ablation ICP-MS. *Geochem Geophys Geosyst.* <https://doi.org/10.1029/2011GC003890>
- Kendrick J, Indares A (2017) The reaction history of kyanite in high-P aluminous granulites. *J Metamorph Geol* 36:125–146. <https://doi.org/10.1111/jmg.12286>
- King J, Harris NBW, Argles TW, Parrish R, Zhang H (2011) Contribution of crustal anatexis to the tectonic evolution of Indian crust beneath southern Tibet. *Bull Geol Soc Am* 123:218–239. <https://doi.org/10.1130/B30085.1>
- Kriegsman LM (2001) Partial melting, partial melt extraction and partial back reaction in anatectic migmatites. *Lithos* 56:75–96. [https://doi.org/10.1016/S0024-4937\(00\)00060-8](https://doi.org/10.1016/S0024-4937(00)00060-8)
- Lanari P (2019) An introduction to XMapTools. User Guide. 2019-12-12
- Lanari P, Vidal O, De Andrade V et al (2014) XMapTools: a MATLAB©-based program for electron microprobe X-ray image processing and geothermobarometry. *Comput Geosci* 62:227–240. <https://doi.org/10.1016/j.cageo.2013.08.010>
- Lee J, Hacker BR, Wang Y (2004) Evolution of North Himalayan gneiss domes: structural and metamorphic studies in Mabja Dome, southern Tibet. *J Struct Geol* 26:2297–2316. <https://doi.org/10.1016/j.jsg.2004.02.013>
- Müller A, René M, Behr HJ, Kronz A (2003) Trace elements and cathodoluminescence of igneous quartz in topaz granites from the Hub Stock (Slavkovský Les Mts., Czech Republic). *Miner Petrol* 79:167–191. <https://doi.org/10.1007/s00710-003-0238-3>
- Müller A, van den Kerkhof AM, Selbekk RS, Broekmans MATM (2016) Trace element composition and cathodoluminescence of kyanite and its petrogenetic implications. *Contrib Miner Petrol* 171:70. <https://doi.org/10.1007/s00410-016-1280-6>
- Najman Y, Appel E, Boudagher-Fadel M, Bown P, Carter A, Garzanti E, Godin L, Han J, Liebke U, Oliver G, Parrish R, Vezzoli G (2010) Timing of India-Asia collision: Geological, biostratigraphic, and palaeomagnetic constraints. *J Geophys Res* 115:1–18. <https://doi.org/10.1029/2010JB007673>
- Neiva AMR (1984) Chromium-bearing kyanite from Mozambique. *Mineral Mag* 48:563–564. <https://doi.org/10.1180/minmag.1984.048.349.18>
- Pagel M, Barbin V, Blanc P, Ohnenstetter D (2000) Cathodoluminescence in geosciences: an introduction. *Cathodoluminescence Geosci.* [https://doi.org/10.1007/978-3-662-04086-7\\_1](https://doi.org/10.1007/978-3-662-04086-7_1)
- Paton C, Hellstrom J, Paul B et al (2011) Iolite: freeware for the visualisation and processing of mass spectrometric data. *J Anal at Spectrom* 26:2508. <https://doi.org/10.1039/c1ja10172b>
- Pattison DRM, Spear FS (2018) Kinetic control of staurolite–Al<sub>2</sub>SiO<sub>5</sub> mineral assemblages: Implications for Barrovian and Buchan metamorphism. *J Metamorph Geol* 36:667–690. <https://doi.org/10.1111/jmg.12302>

- Pearson GR, Shaw DM (1960) Trace elements in kyanite, sillimanite and andalusite. *Am Mineral* 45:808–817
- Peterman EM, Jercinovic MJ, Beane RJ, de Wet CB (2021) Kyanite preserves prograde and retrograde metamorphic events as revealed by cathodoluminescence, geochemistry, and crystallographic orientation. *J Metamorph Geol*. <https://doi.org/10.1111/jmg.12593>
- Prince CI, Harris NBW, Vance D (2001) Fluid-enhanced melting during prograde metamorphism. *J Geol Soc* 158:233–241. <https://doi.org/10.1144/jgs.158.2.233>
- Raimondo T, Payne J, Wade B et al (2017) Trace element mapping by LA-ICP-MS: assessing geochemical mobility in garnet. *Contrib Miner Petrol*. <https://doi.org/10.1007/s00410-017-1339-z>
- Ramseyer K, Mullis J (2000) Geologic application of cathodoluminescence of silicates. *Cathodoluminescence in geosciences*. Springer, Berlin Heidelberg, pp 177–191
- Rubatto D, Chakraborty S, Dasgupta S (2013) Timescales of crustal melting in the Higher Himalayan Crystallines (Sikkim, Eastern Himalaya) inferred from trace element-constrained monazite and zircon chronology. *Contrib Min Pet* 165:349–372. <https://doi.org/10.1007/s00410-012-0812-y>
- Sawyer EW (1999) Criteria for the recognition of partial melting. *Phys Chem Earth Part A Solid Earth Geod* 24:269–279. [https://doi.org/10.1016/S1464-1895\(99\)00029-0](https://doi.org/10.1016/S1464-1895(99)00029-0)
- Schertl H-P, Neuser RD, Sobolev NV, Shatsky VS (2004) UHP-metamorphic rocks from Dora Maira/Western Alps and Kokchetav/Kazakhstan: New insights using cathodoluminescence petrography. *Eur J Mineral* 16:49–57. <https://doi.org/10.1127/0935-1221/2004/0016-0049>
- Tarantola A, Voudouris P, Eglinger A et al (2019) Metamorphic and metasomatic kyanite-bearing mineral assemblages of thassos island (Rhodope, Greece). *Minerals* 9:252. <https://doi.org/10.3390/Min9040252>
- Ubide T, McKenna CA, Chew DM, Kamber BS (2015) High-resolution LA-ICP-MS trace element mapping of igneous minerals: in search of magma histories. *Chem Geol* 409:157–168. <https://doi.org/10.1016/j.chemgeo.2015.05.020>
- Ulrich T, Kamber BS, Jugo PJ, Tinkham DK (2009) Imaging element-distribution patterns in minerals by laser ablation—inductively coupled plasma—mass spectrometry (LA-ICP-MS). *Can Mineral* 47:1001–1012. <https://doi.org/10.3749/canmin.47.5.1001>
- Vernon RH (2011) Microstructures of melt-bearing regional metamorphic rocks. *Mem Geol Soc Am* 207:1–11. [https://doi.org/10.1130/2011.1207\(01\)](https://doi.org/10.1130/2011.1207(01))
- Visonà D, Carosi R, Montomoli C, Tiepolo M, Peruzzo L (2012) Miocene andalusite leucogranite in central-east Himalaya (Everest-Masang Kang area): Low pressure melting during heating. *Lithos* 144–145:194–208. <https://doi.org/10.1016/j.lithos.2012.04.012>
- Vielzeuf D, Holloway JR (1988) Experimental determination of the fluid-absent melting relations in the pelitic system. *Contrib Miner Petrol* 98(3):257–276. <https://doi.org/10.1007/BF00375178>
- Weinberg RF (2016) Himalayan leucogranites and migmatites: nature, timing and duration of anatexis. *J Metamorph Geol* 34:821–843
- Whitney DL, Evans BW (2010) Abbreviations for names of rock-forming minerals. *Am Miner* 95:185–187. <https://doi.org/10.2138/am.2010.3371>
- Wojtowicz AJ (1991) Luminescence of Cr<sup>3+</sup> in kyanite. *J Lumin* 50:221–230. [https://doi.org/10.1016/0022-2313\(91\)90046-X](https://doi.org/10.1016/0022-2313(91)90046-X)
- Yang P, Rivers T (2001) Chromium and manganese zoning in pelitic garnet and kyanite: spiral, overprint, and oscillatory (?) zoning patterns and the role of growth rate. *J Metamorph Geol* 19:455–474. <https://doi.org/10.1046/j.0263-4929.2001.00323.x>
- Zen EA (1988) Phase relations of peraluminous granitic rocks and their petrogenetic implications. *Ann Rev Earth Planet Sci* 16:21–51. <https://doi.org/10.1146/annurev.ea.16.050188.000321>

**Publisher's Note** Springer Nature remains neutral with regard to jurisdictional claims in published maps and institutional affiliations.